Supporting Information for

"A Prototype for Remote Monitoring of Ocean Heat Content"

D. S. Trossman,[1] R. H. Tyler[2,3]

[1]Oden Institute for Computational Engineering and Sciences, University of Texas, Austin, TX, USA

[2]Geodesy and Geophysics Laboratory, Code 61A, NASA Goddard Space Flight Center, Greenbelt, MD, USA

[3]Joint Center for Earth Systems Technology, University of Maryland, Baltimore County, MD, USA

Contents

Models and electromagnetic field calculations

0.1 Ocean state estimation framework

The modeling system used to generate the data analyzed for the purpose of this study is briefly described here. We utilize a re-run of the latest version of the Estimating the Circulation & Climate of the Ocean (ECCO) framework, which is based on the Massachusetts Institute of Technology general circulation model (MITgcm) from 1992 to 2015 [*Fukumori et al.*, 2017]. The ECCO framework reconstructs the history of the ocean over the recent satellite era by filling in the gaps of incomplete observations in a dynamically and kinematically consistent manner [*Stammer et al.*, 2016] using the MITgcm and its adjoint-based data assimilation capabilities. Initial conditions and model parameters for the MITgcm runs performed here are determined by ECCO-Production, version 4 in revision 3 (ECCOv4r3; *Fukumori et al.*, 2017). The MITgcm uses the so-called LLC90 grid, which is at a nominal 1° (0.5^o at equator) resolution with 50 vertical levels. The model features curvilinear Cartesian coordinates (*Forget et al.*, 2015 - see their Figs. 1-3), rescaled height coordinates [*Adcroft and Campin*, 2004], and a partial cell representation of bottom topography [*Adcroft et al.*, 1997]. The MITgcm uses a dynamic/thermodynamic sea ice component (*Menemenlis et al.*, 2005; *Losch et al.*, 2010; *Heimbach et al.*, 2010) and a nonlinear free surface with freshwater flux boundary conditions [*Campin et al.*, 2004]. The wind speed and wind stress are specified as 6-hourly varying input fields over a 24

year period (1992-2015). There are 14-day adjustments to the wind stress, wind speed, specific humidity, shortwave downwelling radiation, and surface air temperature. These adjustments are based on estimated prior uncertainties for the chosen atmospheric reanalysis [*Chaudhuri et al.*, 2013], which is ERA-Interim [*Dee et al.*, 2011]. The net heat flux is then computed via a bulk formula.

The least squares problem solved by the ECCO framework utilizes the method of Lagrange multipliers through iterative improvement, which relies upon a quasi-Newton gradient search [*Nocedal*, 1980; *Gilbert and Lemarechal*, 1989]. The tangent linear model (Jacobian) and its transpose (the adjoint) are needed to solve for the Lagrange multipliers. Algorithmic (or automatic) differentiation tools [*Griewank*, 1992; *Giering and Kaminski*, 1998] have allowed for the practical use of Lagrange multipliers in a time-varying non-linear inverse problem such as the one for the ocean because the discretized adjoint equations no longer need to be explicitly hand-coded. Each of the data points in the time interval of 1992-2015 is weighted by a best-available estimate of its error variance. The observational data assimilated into the ECCO framework to arrive at the model's objective– to reconstruct the ocean's historical conditions–are discussed in *Wunsch and Heimbach* [2013]. These data include satellite-derived ocean bottom pressures, sea ice concentrations, sea surface temperatures, sea surface salinities, sea surface height anomalies, and mean dynamic topography, as well as profiler- and mooring-derived temperatures and salinities [*Fukumori et al.*, 2017]. The control variables that are solved for by ECCO include the initial condition of the velocities, sea surface heights, temperatures, and salinities; time-mean three-dimensional Redi [*Redi*, 1982] coefficients, Gent-McWilliams [*Gent and McWilliams*, 1990] coefficients, and vertical diffusivities [*Gaspar et al.*, 1990]; and time-varying two-dimensional surface forcing fields. Fifty-nine iterations in the optimization run of ECCO were performed to arrive at the solution we start from. Schemes for calculating the conductivity and specific heat at each time step as the model runs are taken from the TEOS-10 package [*MacDougall and Barker*, 2011]. The relationship of the conductance and conductivity transport to electromagnetic fields is described below.

0.2 Calculation of electromagnetic fields

Ohm's Law for a moving conductor,

$$\mathbf{J} = \sigma \left(\mathbf{E} + \mathbf{u} \times \mathbf{F} \right), \tag{1}$$

is a vector equation describing the electric current density $\mathbf{J}$ generated by an electric field $\mathbf{E}$ and/or the velocity $\mathbf{u}$ of the conducting fluid as it moves through the magnetic field $\mathbf{F}$, which we take to be the prescribed background main magnetic field; the total magnetic field $\mathbf{B} = \mathbf{F} + \mathbf{b}$ includes a component $\mathbf{b}$ associated with $\mathbf{J}$ that is neglected in this equation. When the flow velocity is not considered, (1) reduces to $\mathbf{J} = \sigma\mathbf{E}$, and the electrical conductivity σ can be observed as simply the ratio of $\mathbf{J}$ and $\mathbf{E}$, as might be obtained from in situ measurements, for example. Alternatively, in experiments where σ is observed, one may infer instead the flow velocity components $\mathbf{u}$. Hence, it is fairly direct to see how in situ electromagnetic (EM) observations can be used to infer or constrain ocean conductivity and/or velocity.

As the first departure from these truly in situ observations, one can describe configurations where EM observations on the seafloor, for example, can be used to estimate bulk integrated ocean parameters. Consider a controlled electric current source on the seafloor and assume the cable/antenna length is of a scale exceeding that of the ocean thickness. The electrical currents return throughout the water column and their amplitude will be modulated by any changes in the conductance. We see then a potential observational advantage as this seafloor system can be used to monitor depth integrated ocean parameters. Where the conductivity fluctuates due to change in water temperature, for example, this system could be regarded as a bulk thermometer of ocean temperature. Using an alternating current source to remove problems such as electrode drift, very high accuracy could be achieved. One would likely operate this system at frequencies low enough such that the ocean appears "electrically thin," meaning that the electromagnetic wavelengths in the ocean are much larger than the ocean thickness such that the return electric currents reach through the water column as described. The associated period increases with conductance, and therefore typically also with ocean thickness, but does not exceed 10 minutes even in the thickest ocean regions [*Tyler*, 2017].

One need not, however, have in situ or seafloor observations of $\mathbf{J}$ and $\mathbf{E}$ in order to make parameter estimates. Maxwell's equations can be combined with (1) into a governing electromagnetic induction equation:

$$\partial_t \mathbf{B} = \nabla \times \left[\mathbf{u} \times \mathbf{B} - \frac{1}{\mu_0 \sigma} \nabla \times \mathbf{B} \right], \tag{2}$$

where μ_0 is the vacuum permeability constant. Here the opportunity for inferring the ocean parameters σ, $\mathbf{u}$ from remote observations of $\mathbf{B}$ is expressed. Specialized forms of

the induction equation appropriate for large scales near the Earth's surface are described in detail in *Tyler* [2017]. Even when due to electric currents within the ocean, the magnetic fields pass through sea ice and can reach satellite altitudes. But because of geometric attenuation away from the sources, the fields associated with features having length scales much smaller than the satellite altitude will be reduced. Hence, the remote magnetic fields mostly describe depth-integrated, large-scale ocean features. One can see in the specialized forms of the induction equation [*Tyler*, 2017] that the ocean parameters that are potentially inferred are the conductance $\Sigma = \int_h \sigma \, dr$ and the conductivity transport $\mathbf{T}_\sigma = \int_h \sigma \mathbf{u} \mathbf{dr}$.

One can regard the electric currents in the ocean (and their associated magnetic fields which reach beyond the ocean) as generated by either a time-dependent component of the magnetic field incident on the ocean surface, or as due to the ocean flow whereby a small part of the flow's kinetic energy is spent driving these currents. The first process is referred to as electromagnetic 'induction' and a very common application involves magnetic fields incident on the ocean due to electric currents in the ionosphere and magnetosphere. One can regard the induction process as one where electric currents at one location (e.g. the ionosphere) entrain electric currents in another conductor (e.g. the ocean) through the connection of their Coulomb clouds which can reach over great distance and even through insulators. The second process is referred to as 'motional induction' and can be loosely regarded as due to the tendency of a moving electrical conductor to entrain a permeating magnetic field. In the case of a perfect conductor, the magnetic field is regarded as 'frozen in' and moves with the conductor. The 'frozen in' scenario is not typically achieved in ocean applications as the conductivity is not high enough to reduce the importance of the magnetic diffusion term (the last term in (2)).

Finally, for the purposes of this paper it should be noted that while Σ is a parameter potentially recoverable from either induction or motional induction processes, $\mathbf{T}_\sigma$ can be recovered/constrained only in processes of motional induction. Because Σ and $\mathbf{T}_\sigma$ might be inferred in different and varying conditions that also involve a range of expected errors, in this study we shall consider the addition of Σ and $\mathbf{T}_\sigma$ to the GAM separately and with prescribed reference error levels.

0.3 Generalized Additive Model specification

We present scatterplots of the 1992-2015 averages of the ocean heat content (OHC) versus each of its potential predictors in Fig. S1, including the aforementioned electromagnetic variables. The strongest correlation is between OHC and the seafloor depth (Fig. S1a). There is a fairly good correlation between OHC and sea surface height anomaly, as has been noted in previous studies (Fig. S1b). There is a strong correlation between OHC and both bottom pressure (Fig. S1c) and conductance (Fig. S1d). Ekman transport convergence is known to be related to ocean heat uptake [*Buckley et al.*, 2015] and the divergence of the conductivity transport, $\nabla \cdot \mathbf{T}_\sigma$, is related to heat transport convergence through the velocity field. It is expected that $\nabla \cdot \mathbf{T}_\sigma$ would be related to the time rate of change in OHC, not OHC itself. This is true in the ECCO output, as $\nabla \cdot \mathbf{T}_\sigma$ is poorly correlated with OHC (Fig. S1e), and is therefore excluded from the rest of our analysis. Each individual component of $\mathbf{T}_\sigma$ is poorly correlated with OHC, but a marginally fair correlation between OHC and $|\mathbf{T}_\sigma|$ (Fig. S1f) justifies the exploratory use of $|\mathbf{T}_\sigma|$ in our GAM. The scatterplots shown in Fig. S1 look virtually identical when either monthly or annual averages of each quantity are considered, and their correlations are qualitatively the same.

This motivates our use of a Generalized Additive Model (GAM) of the form:

$$O\hat{H}C = f_0 + f_1(S\hat{S}H) + f_2(\hat{p}_b) + f_3(\hat{\Sigma}) + f_4(\hat{H}) + f_5(|\hat{\mathbf{T}}_\sigma|) + g(S\hat{S}H, \hat{p}_b, \hat{\Sigma}, \hat{H}, |\hat{\mathbf{T}}_\sigma|) \tag{3}$$

$$S\hat{S}H = SSH(\eta_{fac} + \epsilon_{\eta_{fac}})\theta(\lambda - \lambda_z) + \epsilon_{SSH}$$

$$\hat{p}_b = p_b(m + \epsilon_m) + \epsilon_{p_b}$$

$$\hat{\Sigma} = \Sigma(\mathbf{b} + \epsilon_{\mathbf{b}})\theta(\hat{\mathbf{G}}_\Sigma(\mathbf{b} + \epsilon_{\mathbf{b}})) + \epsilon_\Sigma$$

$$\hat{H} = H + \epsilon_H$$

$$|\hat{\mathbf{T}}_\sigma| = |\mathbf{T}_\sigma(\mathbf{b} + \epsilon_{\mathbf{b}})|\theta(\hat{\mathbf{G}}_{|\mathbf{T}_\sigma|}(\mathbf{b} + \epsilon_{\mathbf{b}})) + \epsilon_{|\mathbf{T}_\sigma|}$$

$$\theta(x) = \begin{cases} 1, & \text{if } x \geq 0 \\ 0, & \text{if } x < 0 \end{cases}$$

where $f_i(\cdot)$ for $i = 0, ..., 6$ are smoother functions, $g(\cdot)$ is the sum of tensor products of each cross-pairwise combination of arguments (i.e., squares of each variable are not included), the $\hat{\ }$ indicates a measurement (without is the truth), the variables with arguments and without a $\hat{\ }$ are derived from the quantities that a satellite measures (arguments being intermediate quantities that are inferred), and ϵ_X indicates measurement error for variable X. SSH is a function of all of the correction factors (η_{fac}) involved in the retrieval algo-

rithm and post-processing from satellite altimetry (e.g., the tides). SSH has been observed over poleward latitudes (λ) of $\lambda_z = 66^o$ for only a subset of the history of satellite altimetry. The bottom pressure p_b is a function of the mass (m) inferred from the retrieval algorithm from satellite gravimetry. The conductance Σ and conductivity transport $\mathbf{T}_\sigma$ are functions of the magnetic field $\mathbf{b}$ inverted from the retrieval algorithm and post-processing from satellite magnetometry; the functions that indicate whether these inversions are possible (when ≥ 0) are represented by $\hat{G}_\Sigma$ and $\hat{G}_{|\mathbf{T}_\sigma|}$ respectively. The accuracy in which Σ and/or $\mathbf{T}_\sigma$ may be estimated from satellite magnetic data has not yet been established, so we only examine sensitivities of the RMSE to example values. To do this for each variable in (3), random noise is selected from a normal distribution with mean zero and standard deviation equal to various levels (ϵ_X in Eq. 3 for each variable X). This noise is added to the predictors in (3) because the satellite data carry the majority of the observational uncertainties. OHC is re-estimated using the GAM approach with the added noise. The standard deviations (i.e., measurement errors) are set to be $\epsilon_{SSH} = 1$ cm, $\epsilon_{p_b} = 2$ bar, $\epsilon_\Sigma = 3$ S, $\epsilon_H = 1$ m, and $\epsilon_{|\mathbf{T}_\sigma|} = 0.5$ S m s^{-1} for the sensitivity calculations.

References

Adcroft, A., C. Hill, J. Marshall (1997), The representation of topography by shaved cells in a height coordinate model, *Mon. Wea. Rev.*, **125**, 2293–2315.

Adcroft, A., J.-M. Campin (2004), Rescaled height coordinates for accurate representation of free-surface flows in ocean circulation models, *Ocean Modelling*, **7**, 269–284.

Buckley, M. W., R. M. Ponte, G. Forget, P. Heimbach (2015), Determining the origins of advective heat transport convergence variability in the North Atlantic, *J. Clim.*, **28**, 3943–3956.

Campin, J.-M., A. Adcroft, C. Hill, J. Marshall (2004), Conservation of properties in a free surface model, *Ocean Modelling*, **6**, 221–244.

Chaudhuri, A. H., R. M. Ponte, G. Forget, P. Heimbach (2013), A comparison of atmospheric reanalysis surface products over the ocean and implications for uncertainties in air-sea boundary forcing, *J. Clim.*, **26**, 153–170.

Dee, D. P., S. M. Uppala, A. J. Simmons, P. Berrisford, P. Poli S. Kobayashi U. Andrae M. A. Balmaseda G. Balsamo P. Bauer P. Bechtold A. C. M. Beljaars L. van de Berg J. Bidlot N. Bormann C. Delsol R. Dragani M. Fuentes A. J. Geer L. Haimberger S. B. Healy H. Hersbach E. V. Hólm L. Isaksen P. Kållberg M. Köhler M. Matricardi A.

P. McNally B. M. Monge-Sanz J.-J. Morcrette B.-K. Park C. Peubey P. de Rosnay C. Tavolato J.-N. Thépaut F. Vitart (2011), The ERA-Interim reanalysis: configuration and performance of the data assimilation system, *Q. J. Royal Met. Soc.*, **137**, 553–597.

Forget, G., J.-M. Campin, P. Heimbach, C. N. Hill, R. M. Ponte, C. Wunsch (2015), ECCO version 4: an integrated framework for nonlinear inverse modeling and global ocean state estimation, *Geosci. Model Dev.*, **8**(10), 3071–3104, doi:10.5194/gmd-8-3071-2015; http://www.geosci-model-dev.net/8/3071/2015/.

Fukumori, I., O. Wang, I. Fenty, G. Forget, P. Heimbach, R. M. Ponte, 2017: ECCO Version 4 Release 3. DSpace@MIT, http://hdl.handle.net/1721.1/110380.

Gaspar, P., Y. Grégoris, J.-M. LeFevre (1990), A simple eddy kinetic energy model for simulations of the oceanic vertical mixing: tests at Station Papa and long-term upper ocean study site, *J. Geophys. Res.*, **95**, 16,179–16,193.

Gent, P. R., J. C. McWilliams (1990), Isopycnal mixing in ocean circulation models, *J. Phys. Oceanogr.*, **20**, 150–155.

Gilbert, J. C., C. Lemarechal (1989), Some numerical experiments with variable-storage quasi-Newton algorithms, *Math. Program.*, **45**, 407–435.

Giering, R., T. Kaminski (1998), Recipes for adjoint code construction, *ACM Transactions on Mathematical Software*, **24**, 437–474.

Griewank, A. (1992), Achieving logarithmic growth of temporal and spatial complexity in reverse automatic differentiation, *Optimization Methods and Software*, **1**:1, 35–54, doi:10.1080/10556789208805505

Heimbach, P., D. Menemenlis, M. Losch, J. M. Campin, C. Hill (2010), On the formulation of sea-ice models. Part 2: Lessons from multi-year adjoint sea ice export sensitivities through the Canadian Arctic Archipelago, *Ocean Modelling*, **33**, 145–158, doi:10.1016/j.ocemod.2010.02.002.

Losch, M., D. Menemenlis, J. M. Campin, P. Heimbach, C. Hill, 2010: On the formulation of sea-ice models. Part 1: Effects of different solver implementations and parameterizations. *Ocean Modelling*, **33**, 129–144, doi:10.1016/j.ocemod.2009.12.008.

McDougall, T. J., P. M. Barker, 2011: Getting started with TEOS-10 and the Gibbs Seawater (GSW) Oceanographic Toolbox, 28pp., SCOR/IAPSO WG127, ISBN 978-0-646-55621-5.

Menemenlis, D., and Coauthors, 2005: NASA supercomputer improves prospects for ocean climate research. *Eos, Trans. Amer. Geophys. Union*, **86**, 95–96.

Nocedal, J. (1980), Updating quasi-Newton matrices with limited storage, *Mathematics of Computation*, **35**(151), 773–782.

Redi, M. H. (1982), Oceanic isopycnal mixing by coordinate rotation, *J. Phys. Oceanogr.*, **12**, 1154–1158.

Stammer, D., M. Balmaseda, P. Heimbach, A. Köhl, A. Weaver, 2016: Ocean data assimilation in support of climate applications: status and perspectives. *Annu. Rev. Mar. Sci.*, **8**, 491–518, 10.1146/annurev-marine-122414-034113.

Tyler, R. H., 2017. Mathematical Modeling of Electrodynamics Near the Surface of Earth and Planetary Water Worlds. Technical Report TM-2017-219022, NASA. https://ntrs.nasa.gov/archive/nasa/casi.ntrs.nasa.gov/2017001127 9.pdf.

Wunsch, C., P. Heimbach (2013), Dynamically and kinematically consistent global ocean circulation and ice state estimates. Ocean Circulation and Climate, 2nd ed. G. Siedler et al., Eds., Elsevier.
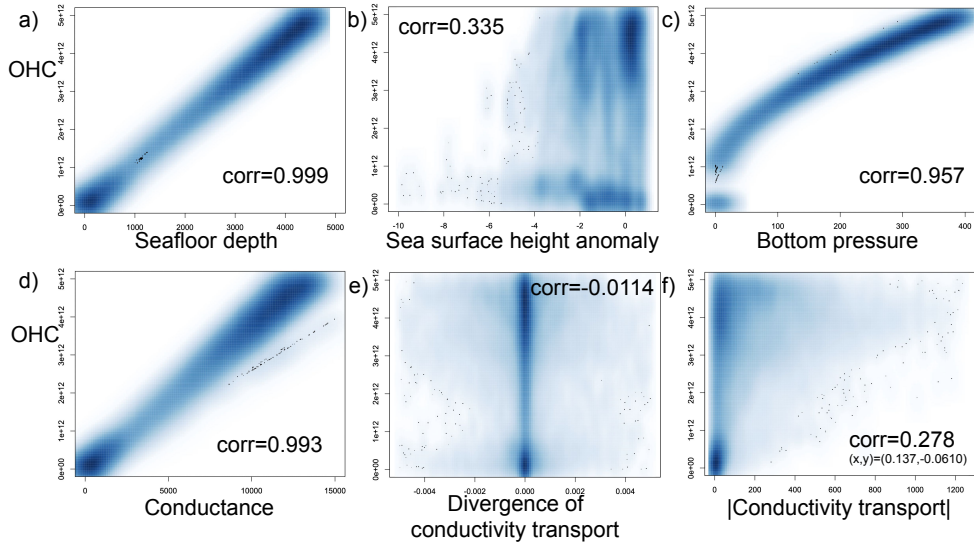
Figure 1. Scatterplots between ocean heat content (OHC - units in J m^{-2}) and (a) the seafloor depths (units in meters), (b) the sea surface heights (units in meters), (c) the bottom pressures (units in bars), (d) the conductances (units in S), (e) the magnitudes of the divergences of the conductivity transports (units in S s^{-1}), and (f) the magnitudes of the conductivity transports (units in S m s^{-1}). The darker blue colors indicate there is a greater density of dots. Also listed are the correlations between each of the quantities plotted (corr).